Photoabsorption, photoionization, and Auger processes at the carbon *K* edge in CH_3I

Ruaridh Forbes,[1,2] Stephen T. Pratt,[3] Alberto De Fanis,[4] Aleksandar R. Milosavljević,[5] Christophe Nicolas,[5] John D. Bozek,[5] Nicholas A. Besley,[6] and David M. P. Holland[7,*]

[1]*Department of Physics and Astronomy, University College London, Gower Street, London WC1E 6BT, United Kingdom*
[2]*Department of Physics, University of Ottawa, 150 Louis Pasteur, Ottawa, Ontario, K1N 6N5 Canada*
[3]*Chemical Sciences and Engineering Division, Argonne National Laboratory, Lemont, Illinois 60439, USA*
[4]*European XFEL GmbH, Holzkoppel 4, 22869 Schenefeld, Germany*
[5]*Synchrotron SOLEIL, l'Orme des Merisiers, Saint-Aubin, BP 48, 91192 Gif-sur-Yvette, France*
[6]*School of Chemistry, University of Nottingham, University Park, Nottingham NG7 2RD, United Kingdom*
[7]*Daresbury Laboratory, Daresbury, Warrington, Cheshire WA4 4AD, United Kingdom*

(Received 30 October 2019; accepted 21 January 2020; published 14 February 2020)

The dynamics of photoabsorption, photoionization, and the associated Auger decay have been investigated at the carbon *K* edge in methyl iodide (CH_3I) using linearly polarized synchrotron radiation. Ion yield measurements were used to investigate transitions in the pre-edge region due to excitations into either unoccupied valence or Rydberg states. The assignment of these transitions was achieved through comparison with theoretical x-ray absorption spectra calculated using time-dependent density functional theory, within the Tamm-Dancoff approximation. Several of the Rydberg states belonging to series converging onto the C1*s* ionization limit exhibit significant vibrational structure that is also interpreted using theoretical calculations. The C1*s* in CH_3I photoelectron spectrum was measured, and the observed vibrational structure was assigned with the aid of theoretical predictions. Polarization dependent, resonantly excited, valence shell photoelectron spectra were recorded at photon energies coinciding with the C $1s \rightarrow \sigma^*$, C $1s \rightarrow 6sa_1$ and C $1s \rightarrow 6pe$ transitions in CH_3I, thereby allowing photoelectron angular distributions to be determined. The nonresonantly excited C(*KVV*) Auger electron spectrum was measured and some of the features observed at high kinetic energies were attributed to transitions into valence orbitals possessing significant iodine character. The contributions of participator and spectator Auger decay to the resonantly excited photoelectron spectra have been assessed. The influence of participator decay appears minor whereas spectator decay results in the enhanced population of satellite states.

DOI: 10.1103/PhysRevA.101.023408

I. INTRODUCTION

Methyl iodide has long been a prototypical sample for photodissociation studies with ultraviolet (UV) light sources [1–9], and it is now playing a similar role in recent photoionization and photodissociation studies with extreme ultraviolet (XUV) light sources and free-electron lasers (FELs) [10–15]. In the latter studies, an electron is excited out of the valence shell by a UV photon, or out of an inner shell by an XUV or x-ray photon, and resonant or nonresonant inner shell excitation is used to probe the resulting dynamics. In principle, the x-ray probe allows the time-dependent relaxation and decay processes to be followed in a site-selective and state-selective manner [16–18]. Knowledge of the electronic structure and spectroscopy of the core excited molecule is particularly valuable for the design of these experiments and for the interpretation of the resulting time-dependent dynamics.

In an attempt to address this need, we have been working to characterize the methyl iodide spectra for excitation out of the inner valence and core orbitals in the photon energy region between 50 and 700 eV. In a series of papers [19–21], we have reported the photoionization, photoelectron, and Auger electron spectra out of the I3*d*, I4*s*, I4*p*, and I4*d* orbitals, complementing these experimental data with theoretical calculations of the corresponding processes. We have also explored the shake-up satellites near the C1*s* edge following nonresonant excitation near 600 eV [22]. In the present paper, we report measurements of the total ion yield curve of CH_3I in the region around the C $1s^{-1}$ edge (291.3 eV) [23]. These data are supported by theoretical calculations of the corresponding absorption spectrum. Comparison of the two data sets allows the assignment of a number of the resonances, along with their corresponding vibrational structure. In principle, the intensities, shapes, and widths of the resonant features can provide insight into the character of the excited state potential energy surfaces and the dynamics on these surfaces. The present data sets are also complemented by measurements of the photoelectron- and Auger-electron energy and angular distributions, both within the continuum and on selected resonances. To our knowledge, this region of the x-ray spectrum of CH_3I has not been studied in detail previously [23–25]. However, CH_3I spectra in this region have been recorded using dipole electron impact techniques, providing a foundation for the present analysis. In addition, previous experimental [26,27] and theoretical [28] studies of the valence shell, single-photon double-photoionization of CH_3I provide invaluable information for the assignment of the present nonresonant and resonant Auger electron spectra.

*david.holland@stfc.ac.uk

The ground state configuration of CH_3I is [25]

$$(I1s)^2(I2s)^2(I2p)^6(C1s)^2(I3s)^2(I3p)^6(I3d)^{10}(I4s)^2(I4p)^6(I4d)^{10} \quad \text{core},$$
$$(1a_1)^2(2a_1)^2 \quad \text{inner valence},$$
$$(1e)^4(3a_1)^2(2e)^4 \quad \text{outer valence},$$

where the core, inner valence, and outer valence configurations are separated. All of the core orbitals except C1*s* are associated with the I atom, while the inner and outer valence orbitals are more delocalized and given labels in the C_{3v} symmetry of the molecule.

Following a discussion of the experimental and theoretical methods, the total ion yield of methyl iodide is presented and compared with the theoretical results. The photoelectron spectra and the nonresonant and resonant Auger spectra following the ejection or excitation of a C1*s* electron in methyl iodide are then presented and discussed. The paper concludes with a discussion of the implications of the present results.

II. EXPERIMENTAL AND THEORETICAL METHODS

A. Experimental apparatus

The experiments were carried out at the French national synchrotron radiation facility SOLEIL, using the soft x-ray undulator-based PLÉIADES beamline. Detailed descriptions of the beamline and end-station spectrometers have been reported previously [29,30], so only a brief description is provided here. The investigation employed a variable groove depth, 600 lines/mm plane grating to monochromatize linearly polarized radiation from an Apple II type permanent magnet undulator. The degree of linear polarization was >99% across the photon energy range considered here, based on beamline estimates and verified at several photon energies by examining the C1*s* in CH_3I photoelectron angular distributions. The monochromator exit slit width depended upon the particular measurement being undertaken. For the ion yield, a slit width of 20 μm was chosen, resulting in a theoretical optical resolution of ~33 meV. A slit width of 50 μm, corresponding to an optical resolution of ~70 meV, was used for the valence shell photoelectron spectra recorded following resonant excitation of the C1*s* orbital in CH_3I. Optical resolutions of ~420 and 100 meV were used for the C(*KVV*) Auger spectrum and the C1*s* photoelectron spectrum, respectively, recorded at a photon energy of 614 eV.

The ion yield was measured using a spectrometer that has been described previously [19]. Commercially available high-purity CH_3I (>99% Sigma Aldrich) was introduced, after several freeze-pump-thaw cycles, into the experimental chamber as an effusive expansion. The experimental chamber pressure was kept close to 4.5×10^{-6} mbar to ensure adequate ion count rates. The ion yield spectra were recorded near the C *K* edge as a function of photon energy in steps of 10 meV in the pre-edge region, and in steps of 200 meV above the ionization threshold. The energy scale was calibrated using the experimental value of 285.62 eV for the C $1s \rightarrow \sigma^*$ transition in CH_3I, determined in previous electron energy loss spectra (EELS) [24].

The Auger electron and photoelectron spectra were recorded using a VG Scienta R4000 hemispherical spectrometer, which was mounted in a fixed position. During the acquisition of spectra, the instrument was operated in the so-called transmission mode of the electron lens. The CH_3I sample gas was introduced inside a differentially pumped gas cell that contained five electrodes to compensate for the plasma potential gradient along the photon beam. This ensured the highest possible spectrometer resolution [30]. The pressure inside the Scienta spectrometer chamber was maintained at around 4×10^{-6} mbar, with the gas cell operating at approximately two orders of magnitude higher. The C(*KVV*) Auger spectrum and the resonantly excited valence shell photoelectron spectra were recorded using an analyzer pass energy of 50 eV and a 0.6 mm curved entrance slit, which resulted in a theoretical spectrometer resolution of 100 meV. An additional contribution to the total experimental resolution arises from the translational Doppler broadening due to the thermal motion of the room temperature CH_3I target. For the highest photoelectron kinetic energy considered here, approximately 300 eV, the Doppler linewidth broadening corresponds to 18 meV [31].

The polarization axis of the linearly polarized radiation entering the monochromator could be rotated through 90°, thereby enabling the determination of the photoelectron angular distributions. Spectra were recorded with the polarization axis lying parallel ($\vartheta = 0°$) and perpendicular ($\vartheta = 90°$) to the direction of the electron's path towards the detector. The resultant intensities, I_0 and I_{90}, respectively, were normalized to the average photon flux (measured with a photodiode located at the end of the beamline), the spectral integration time, and the chamber pressure. The photoelectron anisotropy parameter, β, characterizing the angular distribution, is given by [30]

$$\beta = \frac{2(I_0 - I_{90})}{(I_0 + 2I_{90})}. \quad (1)$$

In the presentation of electron spectra, it is useful to show results that are independent of the electron angular anisotropy, thereby permitting quantities such as branching ratios between various features to be compared directly [30]. This situation can be achieved by constructing the so-called magic angle (54.7° with respect to the polarization of the incident synchrotron radiation) spectra via the well-known expression [30]

$$I_{54.7} = \frac{(I_0 + 2I_{90})}{3}. \quad (2)$$

B. Absorption spectrum calculations

The x-ray absorption spectrum at the C *K* edge in CH_3I was computed using methods similar to those outlined in Ref. [19]. Briefly, the spectrum was calculated by using time-dependent

density functional theory (TDDFT) within the Tamm-Dancoff approximation [32]. The single excitation space was limited to include excitations from the C1s orbital to the full virtual orbital subspace. The calculations utilized the Coulomb attenuating method three-parameter Becke, Lee, Yang, and Parr (CAM-B3LYP) exchange-correlation functional [33] with an augmented quadruple zeta plus polarization basis set [34]. The C K edge ionization threshold relative to the lowest C1s transition energy (C $1s \rightarrow \sigma^*$) in the neutral molecule is computed using a Δ self-consistent field (SCF) approach [35]. With this approach, the energy of the ionization potential is determined to be 6.57 eV above the lowest energy transition. The calculated excitation energy for the C $1s \rightarrow \sigma^*$ transition is 275.09 eV, compared to the experimental value of 285.62 eV [23]. The resulting (shifted) theoretical ionization potential is $285.62 + 6.57 = 292.19$ eV. The pre-edge spectrum (i.e., below the ionization threshold) was generated by convoluting the calculated intensity at each transition energy with a Gaussian function having a full width at half maximum (FWHM) of 0.1 eV.

Vibrationally resolved spectra were computed using the FCclasses code [36] including Franck-Condon (FC) effects. The spectra were simulated at 298 K, but we found the computed spectra to be relatively insensitive to the temperature. Harmonic vibrational frequencies were computed using the B3LYP functional [37] and 6-311++G** basis set. The vibrational frequencies for the core excited states were determined using the maximum overlap method [35] which maintains the core excited state within the DFT calculation. The six vibrational modes of CH_3I may be characterized as follows [38]: $\nu_1(a_1)$ CH_3 symmetrical stretch, $\nu_2(a_1)$ CH_3 symmetrical deformation, $\nu_3(a_1)$ CI stretch, $\nu_4(e)$ CH_3 degenerate stretch, $\nu_5(e)$ CH_3 degenerate deformation, and $\nu_6(e)$ CH_3 rock. See Supplemental Material [39] for vibrational energies and orbital plots of these modes in the neutral ground state, the $6sa_1$, $6pe$, and $6pa_1$ Rydberg states, and the C1s ionic state. The presented spectra were generated by performing a convolution of the vibrational transitions with a Gaussian of 0.06 eV (FWHM).

III. RESULTS AND DISCUSSION

A. Ion yield

Figure 1 shows the ion yield of CH_3I recorded in the vicinity of the C1s pre-edge extending up to and including the ionization threshold. The ion yield is dominated by a series of prominent features which corresponds to resonant excitation of the C1s core electron into unoccupied valence or Rydberg states. The assignment of a specific peak in the experimental spectrum is based upon a visual inspection and on a comparison between the theoretical and measured spectra. This comparison relies upon the calculations predicting the relative energies of the excited states, and the intensities of the transitions, to a sufficiently high degree of accuracy. The theoretical results are shown in Fig. 1 and listed in Table I. The high intensity of peak 8 in the theoretical spectrum is an artifact associated with the theoretical method. The calculated transition energy of the state corresponding to peak 8 is very close to, or slightly higher than, the calculated ionization

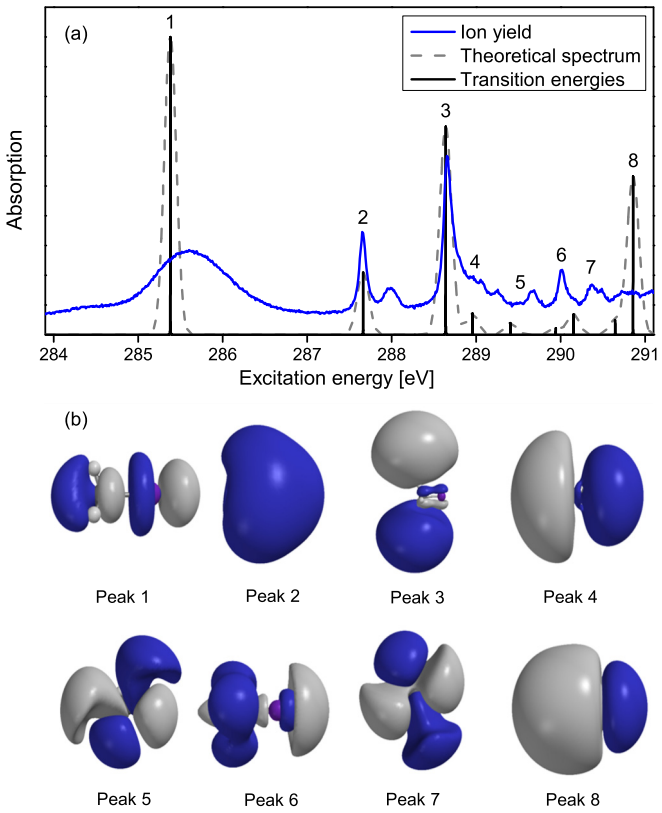

FIG. 1. (a) Experimental ion yield spectrum (blue) of CH_3I recorded in the C1s pre-edge region. The experimental spectrum has been plotted after subtraction of a background signal due to continua associated with ionization of the valence and I4d orbitals. The background signal can be assessed from the wide range ion yield shown in Fig. 2. The experimental spectrum is overlaid with a theoretical absorption spectrum (grey dashes) constructed by convoluting the calculated intensity (black), at each transition energy, with a Gaussian of width 0.1 eV (FWHM). The theoretical spectrum arises solely from excitations of the C1s orbital. The y axis corresponds to the ion yield for the experimental data and to the absorption signal for the theoretical data. In both cases the units are arbitrary. Details of the assignments of the various transitions are provided in the main text and summarized in Table I. (b) Plots of the valence and Rydberg orbitals for peaks 1–8 in panel (a). In the orbital plots, the C-I bond lies horizontally with the methyl group on the left for peaks 1–4, 6, and 8, whereas the methyl group is aligned away from the page for peaks 5 and 7. The blue and grey colors on the orbital plots represent the phase of the wave function.

threshold. The theoretical approach does not allow states lying above the ionization threshold to be distinguished from those lying below. The anomalously high intensity predicted for peak 8 indicates that the state associated with this peak is not being described appropriately. Note that in the theoretical spectrum plotted in Fig. 1 the calculated transition energies have been shifted so that the predicted excitation energy of the C $1s \rightarrow 6sa_1$ transition coincides with the experimental value.

The first intense band, at 285.62 eV, has a large width [$\sim$1 eV (FWHM)], and corresponds to the transition from the C1s orbital into the lowest unoccupied molecular orbital (LUMO) $\sigma^*(a_1)$.The dissociative nature of this core excited

TABLE I. Spectral assignments for the features labeled 1–8 and i–iii in Figs. 1 and 2, respectively. Transition energies and assignments from a previous EELS investigation [24] are provided for comparison.

	Excitation energy (eV)			Hitchcock and Brion [24]	
Feature	Experimental	Theoretical[a]	Assignment	Excitation energy (eV)	Assignment
1	285.62	285.38	$\sigma^*(a_1)$	285.62	$\sigma^*(a_1)$
2	287.66	287.66	$6sa_1$	287.65	$6sa_1$
3	288.66	288.64	$6pe$	288.68	$6pe$
4	289.23	288.96	$6pa_1$	289.25	$6pa_1$
5	289.67	289.41	$5de$	288.68	$7sa_1$
6	290.00	289.94	$5da_1$	290.04	$7p$, $5d$
7	290.37	290.15	$5de$	290.42	$8p$
8	290.7	∼290.8	$7sa_1$	Unobserved	N/A
C1s IP	N/A	292.19	∞	291.3	∞
i	293.4	N/A	Two-electron excitation	293.4	Two-electron excitation
ii	295.6	N/A	Two-electron excitation	295.6	Two-electron excitation
iii	297.4	N/A	Two-electron excitation	Unobserved	N/A

[a]The theoretical transition energies have been shifted so that the calculated value for the C $1s \rightarrow 6sa_1$ transition coincides with the experimental value (287.66 eV).

state has been investigated using *ab initio* molecular dynamics simulations [39]. Similar broad peaks have been observed for the analogous C1s → LUMO transitions in CH_3F, CH_3Cl, and CH_3Br [23,24]. In CH_3I, the width of the C $1s^{-1}\sigma^*$ resonance may be produced by a combination of processes, including ultrafast neutral dissociation, resonant Auger processes, and overlapping states within the resonance. The peaks at higher excitation energies exhibit significantly narrower widths, when compared to that of the $\sigma^*(a_1)$ resonance, and have been attributed to several different Rydberg states [23,24].

The LUMO+1 transition (feature 2) corresponds to excitation into the $6sa_1$ Rydberg state. The nature of this orbital is apparent in the plot shown in Fig. 1(b). The vibrational structure associated with this electronic manifold will be discussed and compared against calculations that include vibrational effects in Sec. III A 1. Features 3 and 4 correspond to transitions into two p-type Rydberg orbitals of $6pe$ and $6pa_1$ character, respectively. These electronic state manifolds also exhibit a significant number of vibrational features (see Sec. III A 2).

The assignment of the higher lying states (features 5–7) becomes increasingly challenging, despite the comparison with the calculated transition energies. However, the plots for features 5, 6, and 7 closely resemble de, da_1, and de orbitals, respectively. Thus, these features are tentatively assigned to the C $1s \rightarrow 5de$, $5da_1$, and $5de$ transitions (Table I). (Note that in C_{3v} symmetry, there are two de orbitals for each value of the principal quantum number, n). Although mixing may occur between the $5da_1$ and $6sa_1$ orbitals, the orbital plot for feature 6 appears to possess significant d character. The orbital plots appear inconsistent with previous assignments of features 6 and 7 to p-type Rydberg states [24]. Angle resolved photoion yield spectra, which can help elucidate the assignment of these higher lying features, have been utilized previously in the study of other small polyatomic molecules [40].

A summary of the experimental and calculated transition energies, as well as the proposed assignments, is provided in Table. I. We note that a weak spectral feature observed at 284.5 eV in Fig. 1 is most likely an artifact due to carbon contamination on the beamline optics. No transition below that due to the C $1s \rightarrow \sigma^*$ excitation is predicted in the present calculation or has been observed previously [23,24].

An ion yield spectrum was recorded with a coarser step size over a broader energy range to investigate the above-threshold continuum structure. This spectrum is shown in Fig. 2, with three weak features appearing at approximately 293.4, 295.6 and 297.4 eV. These features most likely correspond to double excitations. Further details of the shake-up processes at the C K edge of CH_3I have been reported by Trofimov *et al.* [22].

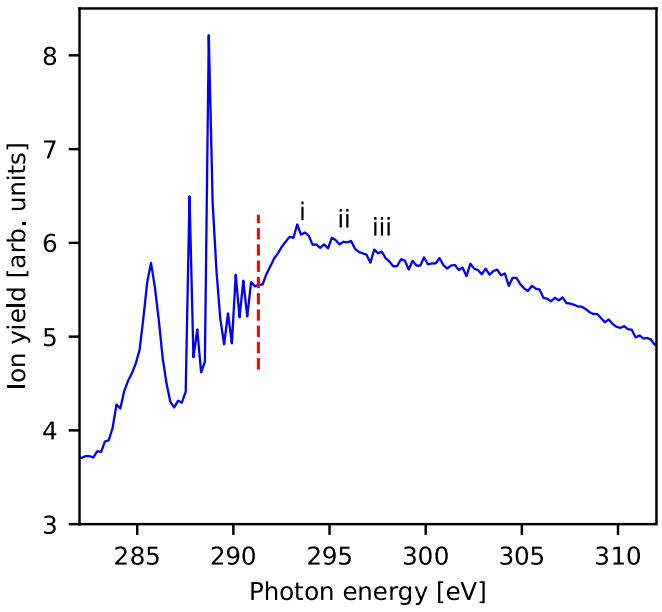

FIG. 2. Experimental ion yield spectrum (blue) of CH_3I in the C1s pre-edge and above threshold regions. The red dashed line denotes the C1s ionization potential taken from Ref. [23]. Highlighted is a weak, but discernible, continuum structure, likely due to double excitations. Transition energies of these features (i–iii) are given in Table I.

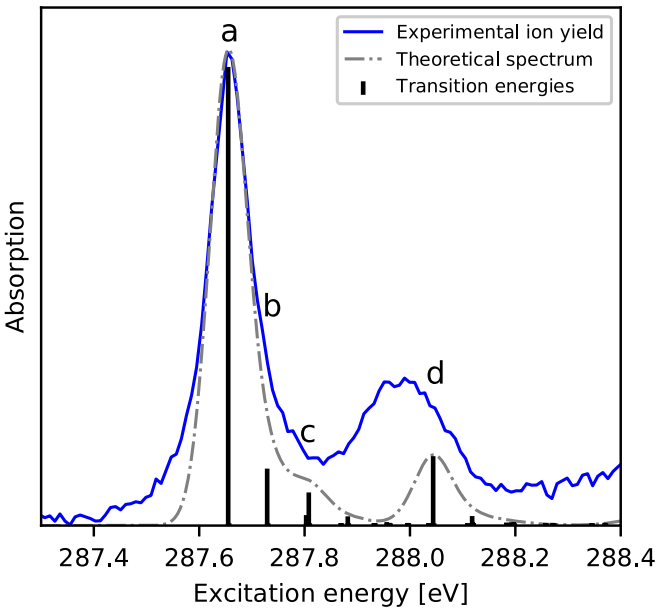

FIG. 3. Experimental ion yield spectrum (blue) of CH_3I in the C1*s* pre-edge region around the 6*s* Rydberg transition and the corresponding theoretical absorption spectrum (grey dot-dash). The theoretical spectrum has been obtained by convoluting the calculated spectral intensity (black) at a particular excitation energy with a Gaussian of 0.06 eV (FWHM). The *y* axis corresponds to the ion yield for the experimental data and to the absorption signal for the theoretical data. In both cases the units are arbitrary. The spectra show some vibrational structure and the dominant transitions are summarized in Table II.

1. Vibrational structure associated with the 6s Rydberg state

The ion yield spectrum in the vicinity of the 6*s* Rydberg state is shown in Fig. 3 to highlight the vibrational structure (labeled a–d) associated with this Rydberg manifold. A relatively sharp peak is observed at ∼287.66 eV, with a shoulder at slightly higher energy (∼287.73 eV). A more diffuse peak appears at an excitation energy 0.32 eV above that corresponding to the adiabatic transition. Some of the calculated structure was observed previously [23,24], but is better resolved in the present spectrum.

Overlaid with the experimental data is a theoretical x-ray absorption spectrum calculated by using the methodology outlined in Sec. II B. The calculated spectrum helps to facilitate the analysis of the experimental spectrum, and the proposed assignments for features a–d in Fig. 3 are given in Table II. We note that the calculated spectrum has been energetically shifted to match the 6*s* band origin so that the vibrational structure can be compared directly. A comparison of the theoretical transition energies with the experimental data indicates that the asymmetry on the high energy side of the peak due to the adiabatic transition, at ∼287.73–287.80 eV, appears to arise mainly from single excitation of the ν_3 mode (feature b) and the ν_2 mode (feature c). The diffuse band labeled d was previously assigned to excitation of one quantum of ν_1, based, in part, on the similarity of the 0.32 eV spacing between features a and d to the CH_3I ground state value of 0.364 eV [38], and the present calculations agree with this assignment. The decrease in the vibrational spacing indicates a weakening of the C-H bond and suggests that the 6*s* Rydberg state is somewhat antibonding in character. However, the *ab initio* molecular dynamics [39] show that this state does not undergo C-I cleavage on an ∼100 fs timescale.

TABLE II. Spectral assignments for the vibrationally resolved components of the 6*s* Rydberg state.

	Excitation energy (eV)		
Feature	Experimental	Theoretical[a]	Assignment
a	287.66	287.66	Band origin (0–0)
b	287.73	287.73	ν_3
c	Unresolved	287.81	ν_2
d	287.98	288.05	ν_1

[a]The theoretical energies have been shifted so that the calculated adiabatic transition energy for the 6*s* Rydberg state (287.90 eV) coincides with the experimental value.

In the experimental spectrum, the width of the band labeled d, associated only with single excitation of the ν_1 mode, is larger than that of the band labeled a. No other electronic transitions are predicted in this region of the spectrum (Fig. 1), the presence of which might account for the observed width. However, there are several factors that could lead to the calculations underestimating the width of the feature around 288 eV. For example, the calculations are based upon a single geometric structure and the vibrational intensities are computed through a Franck-Condon overlap. Higher order effects, such as Herzberg-Teller coupling, are ignored. In view of these approximations, a band width of 60 meV was chosen to provide an adequate representation of the spectra, showing the effects of the vibrational structure on the band profiles.

2. Vibrational structure associated with the 6p Rydberg state

The ion yield spectrum associated with the 6*pe* and 6pa_1 Rydberg manifolds (Fig. 4) exhibits a complex peak structure with numerous vibrational states having spectral overlap and/or significant broadening. The theoretical spectrum for these two states has been shifted so that the adiabatic transitions for the 6*pe* and 6pa_1 states lie at the experimental energies of 288.66 and 289.23 eV, respectively. The calculations take into account the double degeneracy of the 6*pe* state. Table III provides a summary of the dominant vibrational excitations associated with the 6*pe* and 6pa_1 states.

For the 6*pe* state, the electronic symmetry allows vibrational excitations involving the degenerate *e* modes in addition to those arising from the totally symmetric modes. The calculations (Table III) show that only feature B is due solely to excitation of a totally symmetric mode. All the other features, most of which contain contributions from more than one vibrational component, incorporate excitations involving the degenerate modes. Some of the components are combination bands.

The vibrational structure associated with the 6pa_1 state overlaps the high energy part of the structure due to the 6*pe* state. The most intense vibrational transitions associated with the 6pa_1 state (features I, J, and L) arise from excitation of a

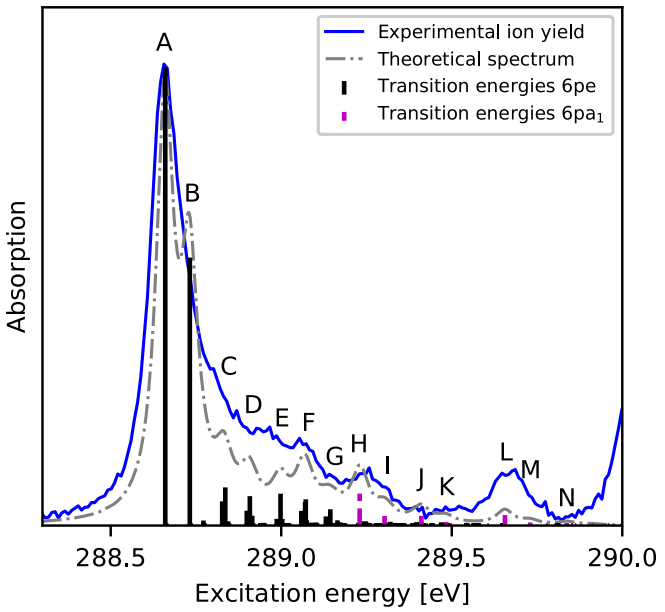

FIG. 4. The experimental ion yield spectrum of CH_3I in the C1*s* pre-edge region around the $6pe$ and $6pa_1$ Rydberg states (blue curve). Both Rydberg manifolds exhibit significant vibrational structure, and assignments for the dominant transitions (A–N) are given in Table III. The theoretical calculations that provide both the transition energy and predicted intensity for the $6pe$ and $6a_1$ states are shown as black and magenta vertical bars, respectively. A convolution of the predicted transitions with a Gaussian function with a width of 0.06 eV is shown as a grey dot-dash curve. The *y* axis corresponds to the ion yield for the experimental data and to the absorption signal for the theoretical data. In both cases the units are arbitrary.

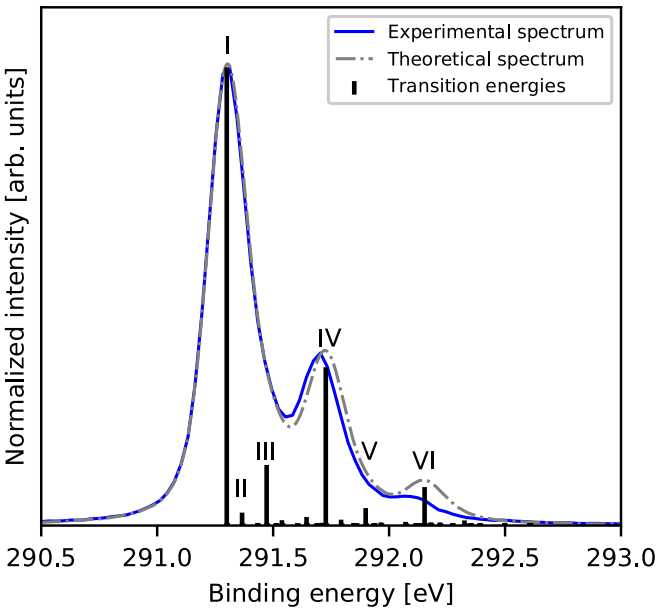

FIG. 5. The experimental vibrationally resolved photoelectron spectrum of C1*s* ionization of CH_3I at 614 eV (blue curve). The theoretical transition energies and intensities from the present calculations are shown as black lines. The convolution of the predicted transitions (see text for details) is also shown (grey dot-dash curve).

single quantum of the ν_3, ν_2, or ν_1 modes, all of which have a_1 symmetry. Overall, the theoretical spectrum derived from the calculated transition energies and intensities provides a satisfactory description of the experimental spectrum due to the $6pe$ and $6pa_1$ states.

TABLE III. Spectral assignments for the dominant vibrational components associated with the $6pe$ and $6pa_1$ Rydberg states.

Feature	Excitation energy (eV)[a]	Vibrational assignments
$6pe$		
A	288.66	0–0
B	288.73	$1\nu_3$
C	288.83	$1\nu_2$, $1\nu_{5a}$
D	288.90	$1\nu_2+1\nu_3$, $1\nu_3+1\nu_{5a}$
E	289.00	$1\nu_{4a}$
F	289.07	$1\nu_1$, $1\nu_3+1\nu_{4a}$, $1\nu_{4b}+1\nu_6$
G	289.14	$1\nu_1+1\nu_3$, $1\nu_{4b}+1\nu_{6a}+1\nu_{6b}$
$6pa_1$		
H	289.23	0–0
I	289.30	$1\nu_3$
J	289.41	$1\nu_2$
K	289.48	$1\nu_2+1\nu_3$
L	289.66	$1\nu_1$
M	289.73	$1\nu_1+1\nu_3$
N	289.84	$1\nu_1+1\nu_2$

aThe calculated excitation energies have been shifted so that the adiabatic transitions for the $6pe$ and $6pa_1$ states coincide with the experimental energies of 288.66 and 289.23 eV, respectively.

B. Carbon 1*s* photoionization

Figure 5 shows the C1*s* photoelectron spectrum for CH_3I, recorded at a photon energy of 614 eV using parallel polarized radiation. Overall, the spectrum exhibits structure similar to that in the closely related system CH_3Cl, where only a single vibrational mode was experimentally resolved [41]. The theoretical transition energies and intensities from the present calculations are also shown in Fig. 5, both as a stick spectrum and after convolution. The convolution uses a Gaussian of 149 meV (FWHM), corresponding to the value of the instrumental resolution extracted from the fitting of the experimental spectrum, together with a Lorentzian of 88 meV (FWHM), corresponding to the extracted core-hole lifetime width. The theoretical spectrum has been shifted so that its origin matches that of the experiment.

A weighted least-squares fitting routine was used extract the positions, intensities, and lifetime widths from the experimental spectrum. To reduce the number of fitted parameters, a single lifetime width was used for all of the observed features. For electrons emitted with kinetic energies of several hundred eV, the effects of post collision interaction are expected to be negligible, and it is reasonable to adopt a Lorentzian profile to describe the photoelectron peaks [42]. The Lorentzian profile was then convoluted with a Gaussian to account for the experimental broadening associated with the photon bandwidth and electron spectrometer resolution. The results from this fitting of the experimental photoelectron spectrum are compared with the theoretical results in Tables IV and V, and a very satisfactory agreement has been found.

TABLE IV. Spectral assignments and binding energies for the C1*s* photoelectron spectrum in methyl iodide.

Feature	Assignment	Binding energy (eV)		Intensity (arb. units)	
		Experimental[a]	Theoretical[b]	Experimental[a]	Theoretical[b]
I	Band origin (0–0)	291.3	291.3	1.0	1.0
II	ν_3	N/A	291.366	N/A	0.023
III	ν_2	291.477	291.472	0.134	0.128
IV	ν_1	291.705	291.727	0.341	0.342
V	$\nu_1 + \nu_2$	291.882	291.899	0.038	0.033
VI	$2\nu_1$	292.110	292.153	0.047	0.079

[a]Experimental binding energy from fit of the present data. The binding energies have been shifted to set the origin at 291.3 eV [23]. See text for details.
[b]Theoretical values from the present calculation. The binding energies have been shifted so that the origin matches the experimental value.

In the absence of vibronic interactions, only totally symmetric (a_1) vibrational modes will be excited in the ionization process. The assignment of the experimental structure has been made through comparison with the theoretical spectrum. In CH_3I, there are only three allowed modes, with energetically distinct vibrational energies, which in the neutral ground state correspond to 364, 155, and 66 meV for the C-H symmetric stretch, H-C-I bend, and C-I stretch, respectively [38]. The dominant progression in Fig. 5 involves the C-H stretching mode, for which the experimental fit gives a fundamental vibrational energy of 405 ± 1 meV. This value is close to the corresponding value for CH_3Cl of 398 meV [41].

The lifetime width extracted from the fit has a value of 88 ± 2 meV. This value is similar to the corresponding lifetime widths for methane (95 ± 5 meV [43]), CO_2 (95 ± 5 meV [44]), CF_4 (77 ± 6 meV [45]), and, perhaps most relevant to the present work, CH_3Cl (88 ± 5 meV [46]). The remarkably similar values among the various species suggests that the core-hole lifetime is relatively insensitive to the local chemical environment [46]. This observation is not surprising given that the dominant Auger processes that determine this lifetime involve inner valence orbitals localized on the C atom.

C. The C(*KVV*) Auger electron spectrum of methyl iodide

The C(*KVV*) Auger electron spectrum of methyl iodide, recorded with parallel polarized synchrotron radiation at a photon energy of 614 eV, is shown in Fig. 6. At this photon energy, the C $1s^{-1}$ photoelectron kinetic energy is high, and the anisotropy parameter characterizing the alignment of the molecular frame is expected to be essentially zero. As a result, the C(*KVV*) Auger electron angular distribution should be isotropic. The C(*KVV*) spectrum of CH_3I, which exhibits several distinct broad peaks, has not been investigated previously, but in some respects it is similar to the extensively studied C(*KVV*) spectrum of CH_4 [47–53]. The latter spectrum is also shown in Fig. 6. We have used the available experimental [48,49,51,52] and theoretical [47,50,53] results for CH_4, along with experimental [26,27] and theoretical [28] determinations of the valence shell double ionization energies of CH_3I, to help guide the assignments for the principal peaks observed in the C(*KVV*) spectrum of CH_3I. We have performed ΔSCF calculations with B3LYP functionals and

TABLE V. Calculated and experimentally extracted vibrational energies for the a_1 symmetry modes in the C1*s* photoelectron spectrum of CH_3I. Vibrational energies in the neutral ground state of CH_3I are provided for comparison [38].

Vibrational mode	Vibrational energy (meV)		
	Experimental[a]	Theoretical[b]	Neutral ground state[c]
ν_1	405 ± 1	426.4	364
ν_2	179 ± 5	172.0	155
ν_3	N/A	65.8	66

[a]From fit of the experimental data. See text for details.
[b]Theoretical results from present calculations.
[c]From Ref. [38].

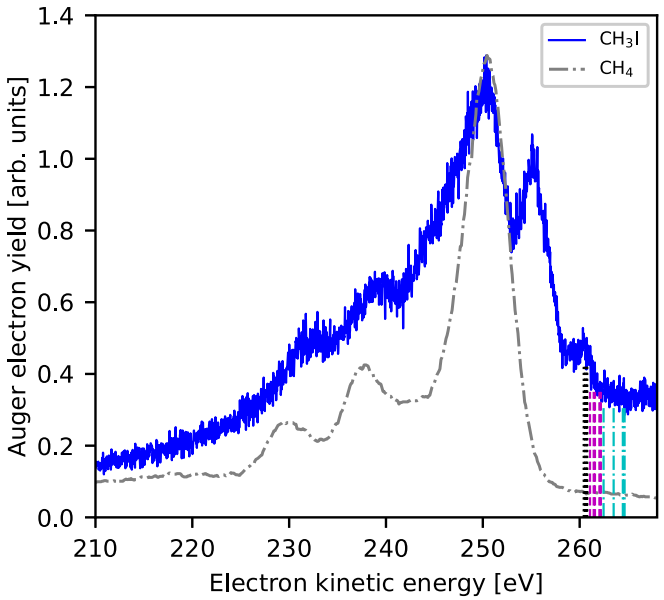

FIG. 6. The Auger electron spectrum following ionization of the *K* shell in CH_3I (blue). The spectrum was recorded at a photon energy of 614 eV, and utilized parallel polarized synchrotron radiation. The dashed vertical lines denote expected kinetic energies for Auger decay transitions correlating with various states of CH_3I^{2+}. Cyan (dot-dash), magenta (long dashes), and black (short dashes) lines refer to methyl iodide doubly ionized states which have varying degrees of CH_3 character; for further details see main text. The CH_3I results are shown alongside the analogous C(*KVV*) Auger electron spectrum of CH_4 (grey dot-dash), data adapted from Ref. [52].

TABLE VI. Theoretical Auger transitions calculated by using the ΔSCF approach with B3LYP functionals and an augmented quadrupole zeta plus polarization basis set.

Final state	Final state multiplicity	Double ionization energy (eV)	Theoretical kinetic energy[b] (eV)	Present expt.[a] electron energy (eV)
$(3a_1)^{-2}$	Singlet	32.83	258.48	260.7
$(1e)^{-1}(3a_1)^{-1}$	Singlet	34.57	256.73	255.1
	Triplet	34.34	256.96	
$(2a_1)^{-1}(3a_1)^{-1}$	Singlet	39.30	252.00	
	Triplet	38.56	252.74	
$(1e)^{-2}$	Singlet (x,y)	38.61	252.69	250.2
	Singlet (x,x)	40.72	250.59	
	Triplet	38.08	253.22	
$(2a_1)^{-1}(1e)^{-1}$	Singlet	41.18	250.12	
	Triplet	40.95	250.34	
$(1a_1)^{-1}(3a_1)^{-1}$	Singlet	43.13	248.17	
	Triplet	42.21	249.09	
$(1a_1)(3a_1)^{-1}$	Singlet	47.51	243.79	238.8
	Triplet	45.79	245.51	
$(2a_1)^{-2}$	Singlet	46.77	244.53	
$(1a_1)^{-2}$	Singlet	55.46	235.84	232.2

[a]Because the Mulliken population analysis indicates that the $2a_1$ orbital is localized primarily on the I atom, we have assumed that it plays only a small role in the C $1s^{-1}$ Auger processes.

[b]The theoretical kinetic energy has been obtained by subtracting the calculated double ionization energy from the experimental value (291.3 eV) of the C $1s$ in CH_3I ionization energy.

an augmented quadruple zeta plus polarization basis for the double valence-hole states of CH_3I^{2+}. These results are shown in Table VI.

A useful model that allows a simple interpretation of an Auger spectrum is that proposed by Siegbahn *et al.* [54]. In this intra-atomic transition model, the Auger decay is assumed to be highly localized around the atomic site containing the initial hole, and the dominant orbitals participating in the deexcitation process are those possessing a high electron density around that site. The delocalized valence orbitals are considered as a linear combination of atomic orbitals, and thus those with a substantial component on the atom containing the initial hole contribute significantly to the Auger transitions. The electronic configuration of methane is $(1a_1)^2(2a_1)^2(1t_2)^6$, and both the $2a_1$ and $1t_2$ orbitals are considered valence orbitals [55]. All three orbitals have substantial C character. As a result, the Auger processes following C $1s^{-1}$ ionization of methane should result in final-state configurations of $(2a_1)^{-2}$, $(2a_1)^{-1}(1t_2)^{-1}$, and $(1t_2)^{-2}$. States with two holes in a single nondegenerate orbital will be singlet, while those with single holes in two different orbitals, or in a degenerate orbital, can be singlet or triplet. If the splittings between the singlets and triplets is small, they will show up as a single peak. Similarly, there are multiple states associated with the $(1t_2)^{-2}$ configuration, but if the splittings among them are small compared to the linewidth, they will result in a single peak. Consistent with this discussion, the methane Auger spectrum in Fig. 6 does indeed show three peaks, at 229.8. 237.7 and 250.4 eV [52], which are assigned to the $(2a_1)^{-2}$, $(2a_1)^{-1}(1t_2)^{-1}$, and $(1t_2)^{-2}$ final states, respectively. The fastest, $(1t_2)^{-2}$, peak is also the most intense, reflecting the greater number of electrons in the t_2 orbital relative to the $2a_1$ orbital.

Based on the Mulliken atomic populations for CH_3I [22], the inner valence $1a_1$ and $2a_1$ orbitals have predominantly C2s and I5s character, respectively. The outer valence $1e$ and $2e$ orbitals have predominantly C2p and I5p character, respectively, while the $3a_1$ orbital corresponds to a σ_{C-I} bonding orbital with an approximately 60/40 mix of I5p and C2p character. Thus, based on the model of Siegbahn *et al.*, the strongest C $1s^{-1}$ Auger processes are expected to be those involving the $1a_1$, $1e$, and $3a_1$ orbitals. In contrast, the $2e$ orbital is essentially a pure I lone-pair orbital, and C $1s^{-1}$ Auger processes involving the $2e$ orbital are expected to be weak. In Table VI, the theoretical Auger electron energies for processes involving the $2a_1$ orbital are included, but these processes are also assumed to be weak in the C1s Auger spectrum because of their dominant I character.

In order of increasing Auger electron energy, one therefore expects CH_3I C $1s^{-1}$ Auger processes to the following six final-state configurations will dominate the spectrum: $(1a_1)^{-2}$, $(1a_1)^{-1}(1e)^{-1}$, $(1a_1)^{-1}(3a_1)^{-1}$, $(1e)^{-2}$, $(1e)^{-1}(3a_1)^{-1}$, and $(3a_1)^{-2}$. The $(1e)^{-2}$ configuration can give rise to multiple states but, as in the case of the $(1t_2)^{-2}$ configuration of CH_4, we assume these splittings are small. Thus, six strong features are expected in the CH_3I C $1s^{-1}$ Auger spectrum. The CH_3I spectrum in Fig. 6 shows considerably more structure than the CH_4 spectrum, but only five fairly well-resolved features are observed, with energies of approximately 232.2, 238.8, 250.2, 255.1, and 260.7 eV. Comparison with the CH_4 spectrum allows the tentative assignment of these features. In particular, given the similarities of the lowest energy feature in the CH_3I and CH_4 spectra, it is reasonable to assign the 232.2 eV feature in the CH_3I spectrum to the $(1a_1)^{-2}$ configuration, which is essentially the $(C2s)^{-2}$ configuration. The peak at

238.8 eV then most likely corresponds to the $(1a_1)^{-1}(1e)^{-1}$ configuration. With this assignment, the state arising from $(1a_1)^{-1}(3a_1)^{-1}$ may correspond to the low energy shoulder of the intense 250.2 eV feature. The $(1e)^{-2}$ configuration would then be responsible for the most intense peak at 250.2 eV, which is consistent with the greater number of electrons in the $1e$ orbital. Finally, the $(1e)^{-1}(3a_1)^{-1}$ and $(3a_1)^{-2}$ configurations would give rise to the 255.1 and 260.7 eV peaks, respectively. As seen in Table VI, these results are in quite good agreement with the predicted energies of the two-hole states, providing support for the assignments.

The experimental results of Hult-Roos *et al.* [27] on the double photoionization of CH_3I provide additional support for the assignment of these last two peaks. In particular, two peaks observed in their spectra have double ionization energies of 34.8 and 31.2 eV. Populating the same two states by Auger processes following C $1s^{-1}$ ionization would lead to Auger electron energies of 256.5 and 260.1 eV, respectively, where we have used a C1s edge energy of 291.3 eV [23]. Given the uncertainties in the measurements, these two energies are quite close to the observed values. Furthermore, Hult-Roos *et al.* suggest that the character of the hole structure is "mainly CH_3 character" and "I and CH_3 character" for the 34.8 and 31.2 eV states, respectively. The $(3a_1)^{-2}$ configuration does indeed have mixed I and CH_3 character, and the $(1e)^{-1}(3a_1)^{-1}$ is mostly CH_3 character, with some I character for the $(3a_1)^{-1}$ hole. These assignments are also in reasonable agreement with the theoretical values in Table VI, i.e., 34.7/34.34 (singlet/triplet) and 32.83, respectively.

Hult-Roos *et al.* [27] and Pilcher-Clayton and Eland [26] also observed a number of doubly ionized states of CH_3I associated with the $(2e)^{-2}$ configuration. Because the $2e$ orbital corresponds closely to an I5p lone-pair orbital, it is not expected that the $(2e)^{-2}$ configuration will be important in the Auger decay of the C $1s^{-1}$ hole. Nevertheless, the electronic configuration of $(3a_1)^2(2e)^2$, corresponding with the doubly charged molecular ion, results in states of $^3A_2$, ^1E, and $^1A_1$ symmetry. The double ionization energy of CH_3I, due to the formation of the $^3A_2$ state, occurs at 26.664 eV [27]. An Auger transition involving this state would lead to the highest electron kinetic energy. An estimated kinetic energy of ~264.6 eV is obtained by using the C1s ionization energy in CH_3I together with the double ionization energy of the $^3A_2$ state. As expected, the C(KVV) spectrum of CH_3I does not exhibit a peak at this kinetic energy.

Pernpointner *et al.* [28] have also calculated the double ionization energies of a number of the states lying in the 25.8–30.1 eV range and given the leading atomic contributions to the individual states. These energies have been used, shifted by 0.84 eV to higher energy so that the calculated double ionization energy (25.82 eV [28]) for the lowest state coincides with the experimental value (26.664 eV [27]), to estimate Auger electron kinetic energies for the C(KVV) transitions. Some of these correspond to the states observed by Hult-Roos *et al.* [27] and Pilcher-Clayton and Eland [26]. The vertical lines shown in Fig. 6, representing predicted Auger electron energies, are color coded according to the atomic contributions [28]: cyan lines correspond to states having a predominantly I5p contribution; magenta lines correspond to states having ~64% I5p, 16% C2p, and 3% H1s character; and black lines correspond to states having ~43% I5p, 22% C2p, and 20% H1s character. It can be seen that only those doubly charged states falling into the third category contribute significantly to the observed intensity distribution. As indicated above, these likely correspond to the $(3a_1)^{-2}$ configuration.

D. Valence shell photoelectron spectra

Polarization dependent, valence shell photoelectron spectra were recorded at photon energies of 285.62, 287.66, and 288.66 eV, coinciding with the C $1s \rightarrow \sigma^*$, C $1s \rightarrow 6sa_1$ and C $1s \rightarrow 6pe$ excitations, respectively. In addition, polarization dependent spectra were measured at a photon energy of 287 eV. This energy does not coincide with a transition into a neutral excited state (Fig. 1). Thus, at this energy, the photoionization dynamics are likely to be dominated by direct ionization.

The nonresonantly excited photoelectron spectrum ($h\nu =$ 287 eV) is very similar to that recorded at a photon energy of 85 eV [56]. The spectrum (Fig. 7) displays well resolved bands due to the $(2e)^{-1}\,\tilde{X}\,^2E$, $(3a_1)^{-1}\,\tilde{A}\,^2A_1$, and $(1e)^{-1}\,\tilde{B}\,^2E$ outer valence states, together with more complex structure associated with the inner valence orbitals. According to Cederbaum *et al.* [57], the single-particle model of ionization breaks down in the inner valence region, and electron correlation redistributes the intensity associated with a particular orbital over numerous satellite states. The photoelectron anisotropy parameters for the single-hole outer valence states, and those for the satellite states, are high ($\beta \geqslant 1$), as is usually the case for direct ionization at high electron kinetic energies.

The photoion yield (Fig. 1) shows that the absorption peaks associated with the C $1s \rightarrow \sigma^*$, C $1s \rightarrow 6sa_1$, and C $1s \rightarrow 6pe$ transitions are superimposed upon continua due to ionization of the valence and I4d orbitals. Thus, the resonantly excited photoelectron spectra of the valence shell, recorded at photon energies coinciding with these resonances, will contain contributions from direct ionization and from indirect processes.

The core excited states may decay through participator or spectator Auger processes [58,59] that result in ions with holes in their valence shells. In a participator Auger decay, the excited electron takes part in the decay: either a valence electron fills the inner hole, and the excited electron is ejected, or the excited electron fills the hole and an electron is ejected from one of the valence orbitals. The end result is the formation of a one-hole (1h) ionic state, and, for CH_3I, these single hole states correspond principally to the $\tilde{X}$, $\tilde{A}$, and $\tilde{B}$ states. The participator Auger decay can affect the photoionization dynamics associated with these ionic states as observed through the photoionization partial cross sections and the photoelectron angular distributions. In a spectator Auger decay, the excited electron remains as a spectator during the decay, a valence electron fills the inner hole, and an electron is ejected from one of the valence orbitals. Such processes lead to the formation of two-hole–one-particle (2h-1p) excited satellite states, which are usually located in binding energy regions higher than those encompassing the single hole states.

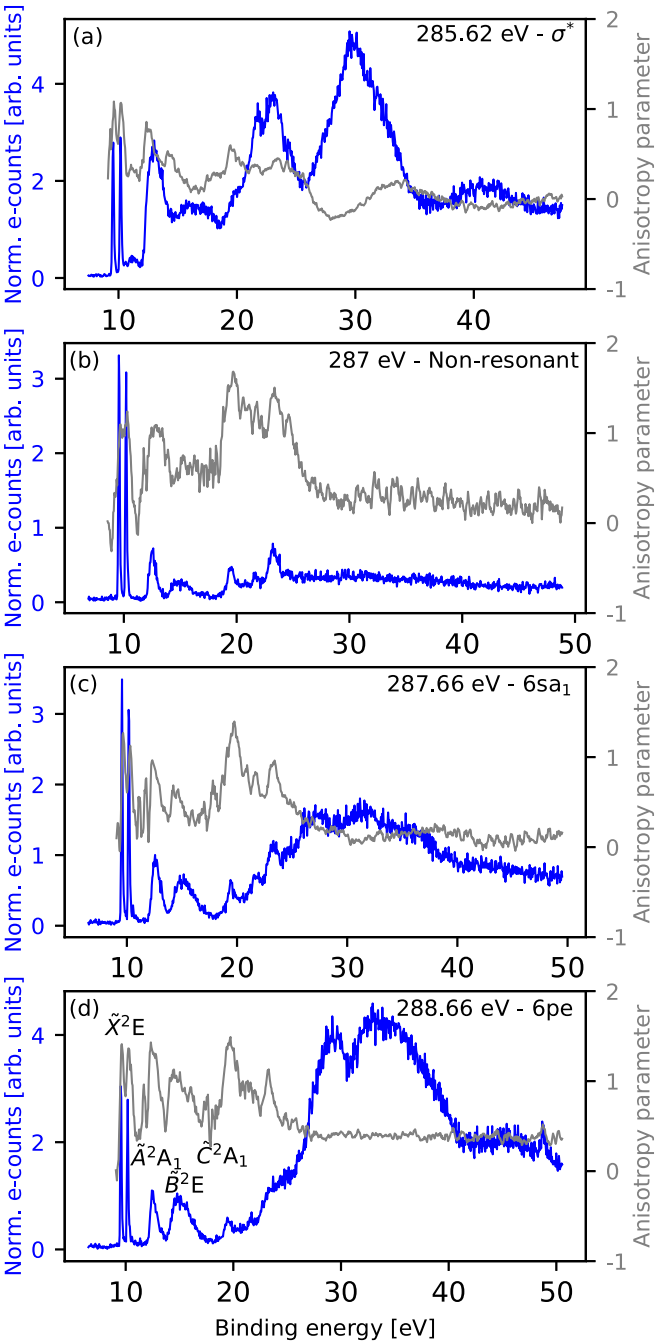

FIG. 7. Magic angle Auger electron spectra (blue), and the associated anisotropy parameters (grey), recorded at photon energies corresponding to the (a) σ^*, (b) nonresonant, (c) $6sa_1$, and (d) $6pe$ transitions in the C1s pre-edge region (see Fig. 1).

We consider first the influence of participator Auger decay on the valence shell photoelectron bands. As already discussed in relation to the C(KVV) spectrum of CH_3I, the probability that the $2e$ outer valence orbital plays a significant role in participator Auger decay is low, as the Mulliken atomic populations for this orbital are dominated by the contribution from the iodine atom. Hence, the overlap between the $2e$ orbital and the core hole is small. The $3a_1$ and especially the $1e$ valence orbitals possess a much higher C character, and thus are more likely to be involved in participator Auger decay.

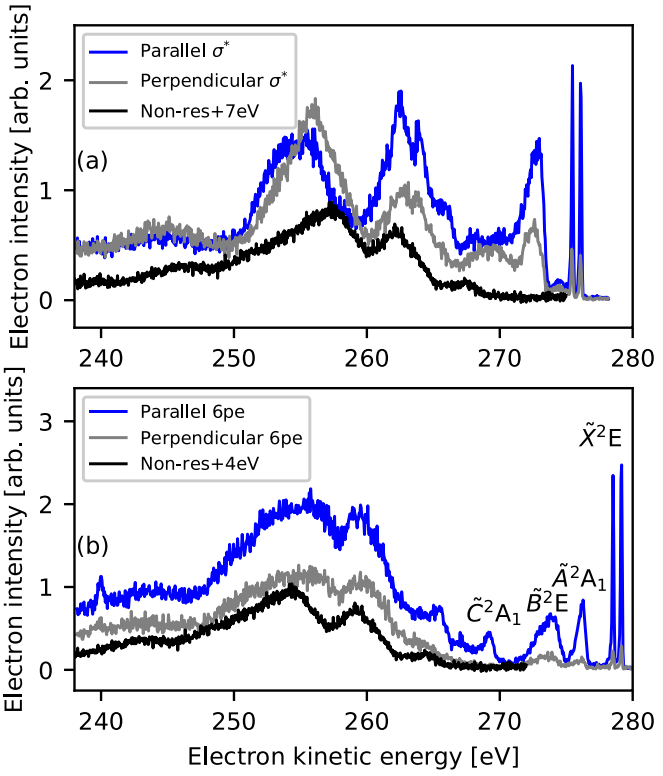

FIG. 8. Resonantly excited Auger electron spectra recorded at photon energies corresponding to the (a) C 1$s \rightarrow \sigma^*$ (285.62 eV) and (b) C 1$s \rightarrow 6pe$ (286.66 eV) transitions for both parallel (blue) and perpendicular (grey) polarization geometries. The nonresonant C(KVV) Auger spectrum (black) is shown for comparison with an appropriate electron kinetic energy shift applied to match the resonant data. The y-axis numbering applies to the resonantly excited (blue and grey) spectra only. The vertical positions of the nonresonant (black) spectra are arbitrary, with the spectra being placed to provide a suitable comparison with the resonantly excited spectra.

Figure 7 shows the magic angle, resonantly excited valence shell photoelectron spectra and the corresponding photoelectron anisotropy parameters derived from the polarization dependent measurements. Neither the relative intensities nor the β values associated with the $\tilde{X}$ single-hole states differ significantly from those in the nonresonantly excited ($h\nu = 287$ eV) spectrum. However, the relative intensities of the $\tilde{A}$ and $\tilde{B}$ bands are strongly dependent on the excitation wavelength. This is consistent with the idea that the hole in the $\tilde{X}$ state is localized on the I atom, while the hole in the $\tilde{A}$ and $\tilde{B}$ states has more density on the C atom. As expected, this behavior complements that observed following resonant excitation of the I4d orbital in CH_3I [21], where participator Auger decay was found to strongly influence the $\tilde{X}\,^2E$ state photoelectron anisotropy parameter. In general, participator Auger decay can also lead to the population of vibrational levels whose direct photoionization cross sections are low.

Turning now to spectator Auger decay, Fig. 8 shows the resonantly excited, polarization dependent, valence shell photoelectron spectra recorded at photon energies of 285.62 and 288.66 eV, coinciding with the C 1$s \rightarrow \sigma^*$ and C 1$s \rightarrow$ 6pe transitions, respectively. These spectra are plotted as a function of electron kinetic energy. A kinetic energy shifted

C(*KVV*) spectrum of CH_3I has been included in each panel of Fig. 8. In a normal (nonresonant) Auger spectrum, the peaks are due to transitions into two-hole (2h) final states. For resonant excitation with the initially excited electron remaining a spectator to the subsequent decay, the peaks in the Auger spectrum arise from transitions into 2h-1p final states. In this case, the resonantly excited Auger spectrum generally resembles the normal Auger spectrum, but the corresponding features are shifted to higher kinetic energy by several eV. This shift is due to the shielding provided by the electron in the excited orbital. For example, the Auger electron kinetic energy associated with the iodine $M_{45}N_{45}N_{45}$ transitions in CH_3I [20] are shifted to higher energy by ~7.62 eV in the resonantly excited spectrum compared to the corresponding values in the normal spectrum. In CH_3I, the term value for the I $3d_{5/2} \rightarrow \sigma^*$ transition is 6.45 eV. Thus, the shift in the Auger kinetic energies is larger than the term value. Similarly, in CH_4, the kinetic energies of the resonantly excited C(*KVV*) spectrum, coinciding with the C $1s \rightarrow 3sa_1$ transition (with a term value of ~3.7 eV [51]) were ~7 eV higher than those in the normal spectrum [52]. The shift in the kinetic energy depends upon the shielding, and hence the term value, and decreases as the excited state approaches the ionization threshold.

Using these experimentally determined shifts as a guide, the C(*KVV*) spectrum in CH_3I has been shifted, somewhat arbitrarily, by 7 eV towards higher kinetic energy for comparison with the valence shell photoelectron spectra recorded at 285.62 eV [Fig. 8(a)] coinciding with the C $1s \rightarrow \sigma^*$ transition, whose term value is 5.68 eV. In Fig. 8(b), the C(*KVV*) spectrum has been shifted to higher kinetic energy by 4 eV, while the term value of the C $1s \rightarrow 6pe$ transition is 2.64 eV. The ordinate scales used for the C(*KVV*) spectra in Figs. 8(a) and 8(b) are arbitrary, and not the same as that for the valence shell photoelectron spectra. Auger electron angular distributions following resonant excitation may be anisotropic [60] due to molecular frame alignment induced by the photoabsorption process. Our discussion of the effect of spectator Auger decay does not consider this possible anisotropy. However, the shifted C(*KVV*) spectra plotted in Fig. 8 are sufficient to allow the influence of spectator Auger decay on the resonantly excited valence shell photoelectron spectra to be assessed.

The evidence presented in Fig. 8 suggests that much of the additional broad structure observed in the inner valence region of the resonantly excited photoelectron spectra can be attributed to spectator Auger decay. Such processes seem to constitute the major contributor to the electron intensity occurring at binding energies greater than that of the $\tilde{C}\,^2A_1$ state band at ~19.5 eV. Note that the sharp peak occurring in the $C1s \rightarrow 6pe$ resonantly excited photoelectron spectrum at a kinetic energy of ~239 eV is due to ionization of the $I3d_{5/2}$ orbital with third-order radiation.

The comparison of the resonantly excited valence shell photoelectron spectra of CH_3I recorded in the present study with the analogous spectra for CH_3Cl measured by Nandi *et al.* [61] is informative. We consider specifically the spectra arising from the C $1s \rightarrow \sigma^*$ and C $1s \rightarrow pe$ transitions. For the spectra associated with the σ^* state, the magic angle photoelectron spectrum in each molecule exhibits a large enhancement of intensity in the inner valence binding energy region with a dip occurring around ~25 eV (Fig. 7). Even the overall shape of the inner valence photoelectron band in CH_3I is similar to that in CH_3Cl. Moreover, the photoelectron anisotropy parameters exhibit a similar dependence on binding energy with the value of the β parameter becoming negative in the ~26–30 eV range (Fig. 7).

Excitation into the *pe* Rydberg state produces a huge increase in the photoelectron intensity in the inner valence region of each molecule, with the associated β parameter being essentially zero (isotropic). This similarity in the analogous resonantly excited valence shell photoelectron spectra of CH_3Cl and CH_3I suggests a common decay mechanism. The C(*KVV*) spectrum of CH_3Cl has not been measured but is likely to be similar to that of CH_3I. Thus, it seems that spectator Auger decay is the dominant deexcitation process for the core excited states, and leads to the formation of numerous 2h-1p states located in the inner valence binding energy region.

The calculations performed by Nandi *et al.* show that the average angular distribution for all the unresolved spectator resonant Auger electrons is almost isotropic, regardless of excitation energy [61]. This prediction appears consistent with the experimental results on both CH_3Cl and CH_3I.

The resonantly excited C1*s* Auger spectra of CH_4 show that the observed structure increasingly resembles that occurring in the normal Auger spectrum as the excited state approaches the ionization threshold [52]. However, at some excitation energies, additional structure is discernible that may be due to vibrational effects. It is possible that such effects may account, at least in part, for the differences between the broad features observed in the resonantly excited photoelectron spectra of CH_3I and those in the C(*KVV*) spectrum.

IV. CONCLUSION

The total ion yield of CH_3I has been measured, using synchrotron radiation, in the vicinity of the C1*s* ionization threshold. Structure observed below the ionization limit has been assigned to transitions into either unoccupied valence or Rydberg orbitals, based upon predicted excitation energies and intensities calculated using TDDFT, within the Tamm-Dancoff approximation. Several of the Rydberg states exhibit vibrational structure. Tentative assignments for the active vibrational modes have been proposed through comparison with a simulated spectrum computed using the FCclasses code. In general, a satisfactory agreement has been achieved between the experimental and calculated vibrational band shapes. Resonantly excited, polarization dependent, valence shell photoelectron spectra have been recorded at photon energies coinciding with the $C1s \rightarrow \sigma^*$, $C1s \rightarrow 6sa_1$ and $C1s \rightarrow 6pe$ transitions. These have allowed magic angle photoelectron spectra and photoelectron anisotropy parameters to be determined. The normal C(*KVV*) spectrum has been measured and some of the structure has been interpreted using previously determined ionization energies of CH_3I and expectations based upon a localized electron density model. This interpretation suggests that, although most of the intensity in the C(*KVV*) spectrum can be associated with molecular orbitals possessing a high C and H character, transitions involving

valence orbitals containing some I contribution may account for some of the peaks occurring at high kinetic energies.

The resonantly excited valence shell photoelectron spectra have been discussed in relation to participator and spectator Auger decay. The influence of participator decay appears minor. In contrast, spectator Auger decay seems to account for the significant increase in the population of 2h-1p states located in the inner valence region. The evidence for this interpretation has been obtained by comparing the normal C(*KVV*) spectrum, shifted to higher kinetic energy to allow for the shielding provided by the excited electron in the resonant state, with the resonantly excited photoelectron spectra. This comparison seems to confirm the dominance of spectator Auger decay.

ACKNOWLEDGMENTS

R.F. is grateful to the Engineering and Physical Sciences Research Council (EPSRC) for support via a research studentship. S.T.P. was supported by the US Department of Energy, Office of Science, Office of Basic Energy Sciences, Division of Chemical Sciences, Geosciences, and Biosciences under Contract No. DE-AC02-06CH11357. N.A.B. is grateful for support from the EPSRC (Grant No. EP/N002148/1). D.M.P.H. is grateful to the Science and Technology Facilities Council (United Kingdom) for financial support. We are grateful to the SOLEIL staff for running the facility and providing beam time under Project No. 20150786.

[1] R. Schinke, *Photodissociation Dynamics* (Cambridge University Press, Cambridge, 1993).
[2] M. N. R. Ashfold and J. E. Baggott (Eds.), *Molecular Photodissociation Dynamics* (Royal Society of Chemistry, London, 1987).
[3] S. J. Riley and K. R. Wilson, Faraday Disc. **53**, 132 (1972).
[4] R. O. Loo, H. P. Haerri, G. E. Hall, and P. L. Houston, J. Chem. Phys. **90**, 4222 (1989).
[5] H. Guo and G. C. Schatz, J. Chem. Phys. **93**, 393 (1990).
[6] A. T. J. B. Eppink and D. H. Parker, J. Chem. Phys. **110**, 832 (1999).
[7] R. de Nalda, J. Durá, A. García-Vela, J. G. Izquierdo, J. González-Vázquez, and L. Bañares, J. Chem. Phys. **128**, 244309 (2008).
[8] S. H. Gardiner, M. L. Lipciuc, T. N. V. Karsili, M. N. R. Ashfold, and C. Vallance, Phys. Chem. Chem. Phys. **17**, 4096 (2015).
[9] R. Boll *et al.*, Struct. Dyn. **3**, 043207 (2016).
[10] A. R. Attar, A. Bhattacherjee, and S. R. Leone, J. Phys. Chem. Lett. **6**, 5072 (2015).
[11] Li Fang, Hui Xiong, E. Kukk, and N. Berrah, Appl. Sci. (Basel) **7**, 529 (2017).
[12] A. Rudenko *et al.*, Nature (London) **546**, 129 (2017).
[13] K. Amini *et al.*, Struct. Dyn. **5**, 014301 (2018).
[14] F. Allum *et al.*, J. Chem. Phys. **149**, 204313 (2018).
[15] F. Braußе *et al.*, Phys. Rev. A **97**, 043429 (2018).
[16] N. Berrah and P. H. Bucksbaum, Sci. Am. **310**, 64 (2014).
[17] P. H. Bucksbaum and N. Berrah, Phys. Today **68**(7), 26 (2015).
[18] L. Young *et al.*, J. Phys. B: At. Mol. Opt. Phys. **51**, 032003 (2018).
[19] R. Forbes *et al.*, J. Chem. Phys. **149**, 144302 (2018).
[20] R. Forbes *et al.*, J. Chem. Phys. **149**, 094304 (2018).
[21] R. Forbes *et al.* (unpublished).
[22] A. B. Trofimov, A. M. Belogolova, S. A. Serebrennikova, R. Forbes, S. T. Pratt, and D. M. P. Holland, J. Chem. Phys. **150**, 224303 (2019).
[23] A. P. Hitchcock and C. E. Brion, J. Electron Spectrosc. Relat. Phenom. **13**, 193 (1978).
[24] A. P. Hitchcock and C. E. Brion, J. Electron Spectrosc. Relat. Phenom. **17**, 139 (1979).
[25] T. N. Olney, G. Cooper, and C. E. Brion, Chem. Phys. **232**, 211 (1998).
[26] A. Pilcher-Clayton and J. H. D. Eland, J. Electron Spectrosc. Relat. Phenom. **142**, 313 (2005).
[27] A. Hult Roos, J. H. D. Eland, D. Koulentianos, R. J. Squibb, L. Karlsson, and R. Feifel, Chem. Phys. **491**, 42 (2017).
[28] M. Pernpointner, J. P. Zobel, E. Fasshauer, and A. N. Sil, Chem. Phys. **407**, 39 (2012).
[29] J. Söderström, A. Lindblad, A. N. Grum-Grzhimailo, O. Travnikova, C. Nicolas, S. Svensson, and C. Miron, New J. Phys. **13**, 073014 (2011).
[30] I. Powis, D. M. P. Holland, E. Antonsson, M. Patanen, C. Nicolas, C. Miron, M. Schneider, D. Yu. Soshnikov, A. Dreuw, and A. B. Trofimov, J. Chem. Phys. **143**, 144304 (2015).
[31] P. Baltzer, L. Karlsson, M. Lundqvist, and B. Wannberg, Rev. Sci. Instrum. **64**, 2179 (1993).
[32] M. Stener, G. Fronzoni, and M. de Simone, Chem. Phys. Lett. **373**, 115 (2003).
[33] T. Yanai, D. P. Tew, and N. C. Handy, Chem. Phys. Lett. **393**, 51 (2004).
[34] L. S. C. Martins, F. A. L. de Souza, G. A. Ceolin, F. E. Jorge, R. C. de Berrado, and C. T. Campos, Comput. Theor. Chem. **1013**, 62 (2013).
[35] N. A. Besley, A. T. B. Gilbert, and P. M. W. Gill, J. Chem. Phys. **130**, 124308 (2009).
[36] F. Santoro, FCclasses: A Fortran 77 Code, http://www.pi.iccom.cnr.it/fcclasses, 2008.
[37] P. J. Stephens, F. J. Devlin, C. F. Chabalowski, and M. J. Frisch, J. Phys. Chem. **98**, 11623 (1994).
[38] T. Shimanouchi, *Tables of Molecular Vibrational Frequencies, Consolidated Volume I*, NSRDS-NBS 39 (U.S. National Bureau of Standards, Washington, 1972).
[39] See Supplemental Material at http://link.aps.org/supplemental/10.1103/PhysRevA.101.023408 for calculated vibrational energies and plots of the corresponding motions, and for molecular dynamics simulations of the C $1s^{-1}\sigma^*$ and C $1s^{-1}6s$ dissociations.
[40] J. Adachi, N. Kosugi, and A. Yagishita, J. Phys. B: At. Mol. Opt. Phys. **38**, R127 (2005).
[41] S. Sundin, L. J. Saethre, S. L. Sorensen, A. Ausmees, and S. Svensson, J. Chem. Phys. **110**, 5806 (1999).
[42] G. B. Armen, J. Tulkki, T. Åberg, and B. Crasemann, Phys. Rev. A **36**, 5606 (1987).

[43] T. X. Carroll, N. Berrah, J. Bozek, J. Hahne, E. Kukk, L. J. Sæthre, and T. D. Thomas, Phys. Rev. A **59**, 3386 (1999).
[44] T. X. Carroll, J. Hahne, T. D. Thomas, L. J. Sæthre, N. Berrah, J. Bozek, and E. Kukk, Phys. Rev. A **61**, 042503 (2000).
[45] T. X. Carroll, K. J. Børve, L. J. Sæthre, J. D. Bozek, E. Kukk, J. A. Hahne, and T. D. Thomas, J. Chem. Phys. **116**, 10221 (2002).
[46] M. G. Zahl, K. J. Børve, and L. J. Sæthre, J. Electron Spectrosc. Relat. Phenom. **185**, 226 (2012).
[47] I. B. Ortenburger and P. S. Bagus, Phys. Rev. A **11**, 1501 (1975).
[48] R. R. Rye, T. E. Madey, J. E. Houston, and P. H. Holloway, J. Chem. Phys. **69**, 1504 (1978).
[49] R. R. Rye, D. R. Jennison, and J. E. Houston, J. Chem. Phys. **73**, 4867 (1980).
[50] F. P. Larkins, L. C. Tulea, and E. Z. Chelkowska, Aust. J. Phys. **43**, 625 (1990).
[51] K. Ueda, M. Okunishi, H. Chiba, Y. Shimizu, K. Ohmori, Y. Sato, E. Shigemasa, and N. Kosugi, Chem. Phys. Lett. **236**, 311 (1995).
[52] A. Kivimäki, M. Neeb, B. Kempgens, H. M. Köppe, and A. M. Bradshaw, J. Phys. B: At. Mol. Opt. Phys. **29**, 2701 (1996).
[53] K. Endo, K. Hyodo, K. Takaoka, T. Ida, S. Shimada, Y. Takagi, and E. Z. Kurmaev, Chem. Phys. **452**, 31 (2015).
[54] H. Siegbahn, L. Asplund, and P. Kelfve, Chem. Phys. Lett. **35**, 330 (1975).
[55] G. Herzberg, *Molecular Spectra and Molecular Structure* (Van Nostrand Reinhold Company, New York, 1996), Vol. III.
[56] D. M. P. Holland, I. Powis, G. Öhrwall, L. Karlsson, and W. von Niessen, Chem. Phys. **326**, 535 (2006).
[57] L. S. Cederbaum, W. Domcke, J. Schirmer, and W. von Niessen, Adv. Chem. Phys. **65**, 115 (1986).
[58] V. Schmidt, *Electron Spectrometry of Atoms using Synchrotron Radiation* (Cambridge University Press, Cambridge, 1997).
[59] G. B. Armen, H. Aksela, T. Åberg, and S. Aksela, J. Phys. B: At. Mol. Opt. Phys. **33**, R49 (2000).
[60] D. Dill, J. R. Swanson, S. Wallace, and J. L. Dehmer, Phys. Rev. Lett. **45**, 1393 (1980).
[61] S. Nandi, C. Nicolas, A. N. Artemyev, N. M. Novikovskiy, C. Miron, J. D. Bozek, and Ph. V. Demekhin, Phys. Rev. A **96**, 052501 (2017).